AAAS
Research
Volume 2020, Article ID 5958243, 10 pages
https://doi.org/10.34133/2020/5958243

Research Article

Atomistic Surface Passivation of $CH_3NH_3PbI_3$ Perovskite Single Crystals for Highly Sensitive Coplanar-Structure X-Ray Detectors

Yilong Song,[1] Liqi Li,[2] Weihui Bi,[1] Mingwei Hao,[1] Yifei Kang,[1] Anran Wang,[1] Zisheng Wang,[1] Hanming Li,[1] Xiaohui Li,[1] Yanjun Fang,[2] Deren Yang,[2] and Qingfeng Dong[1]

[1]*State Key Laboratory of Supramolecular Structure and Materials, College of Chemistry, Jilin University, Changchun 130012, China*
[2]*State Key Laboratory of Silicon Materials and School of Materials Science and Engineering, Zhejiang University, Hangzhou 310027, China*

Correspondence should be addressed to Yanjun Fang; jkfang@zju.edu.cn and Qingfeng Dong; qfdong@jlu.edu.cn

Received 15 May 2020; Accepted 12 August 2020; Published 22 September 2020

Organic-inorganic halide perovskites (OIHPs) are recognized as the promising next-generation X-ray detection materials. However, the device performance is largely limited by the ion migration issue of OIHPs. Here, we reported a simple atomistic surface passivation strategy with methylammonium iodide (MAI) to remarkably increase the ion migration activation energy of $CH_3NH_3PbI_3$ single crystals. The amount of MAI deposited on the crystal surface is finely regulated by a self-assemble process to effectively suppress the metallic lead defects, while not introducing extra mobile ions, which results in significantly improved dark current stability of the coplanar-structure devices under a large electric field of 100 V mm^{-1}. The X-ray detectors hence exhibit a record-high sensitivity above 700,000 μC Gy_{air}^{-1} cm^{-2} under continuum X-ray irradiation with energy up to 50 keV, which enables an ultralow X-ray detection limit down to 1.5 nGy_{air} s^{-1}. Our findings will allow for the dramatically reduced X-ray exposure of human bodies in medical imaging applications.

1. Introduction

High-performance X-ray detectors are increasingly important in many fields, including medical imaging, security monitoring, material inspection, and scientific research. [1–4] Especially in the medical diagnosis field, the X-ray-based medical imaging techniques such as X-ray radiography and computed tomography (CT) are gradually becoming the routine methods for disease diagnosis. However, in view of the cancer risk of high-dose X-ray radiation to the human body, [5, 6] X-ray detectors with much higher sensitivity are urgently needed to enable ultralow-dose X-ray imaging. For a semiconductor-type X-ray detector, which directly converts incident X-ray into electron-hole pairs, the sensitivity of the device is closely related to the attenuation capability and the electrical transport properties of the active material. This requires the material to possess both a high atomic number for large X-ray stopping power and a large mobility-lifetime ($\mu\tau$) product to allow the efficient charge collection. [7] Amorphous Se- (α-Se-) based X-ray imaging sensor has occupied the majority market share of direct conversion-type X-ray detectors for decades. [8] However, its sensitivity is too low to enable ultralow-dose imaging, which is mainly limited by the small atomic number as well as the small $\mu\tau$ product of α-Se.

During the past few years, organic-inorganic halide perovskites (OIHPs) were identified as the promising new-generation candidate semiconductors for X-ray detection due to their outstanding physical and optoelectronic properties compared to the traditional X-ray detection materials like Si, CdZnTe, and α-Se, such as a large atomic number, [9–11] low intrinsic trap density, [12–14] and large $\mu\tau$ product. [9, 15, 16] Moreover, the low material cost and the low-temperature solution processability for high-quality perovskite single crystal (SC) greatly reduce the cost and complexity in device preparation and integration.

Currently, the best OIHP-based X-ray detector, which is reported by Huang et al., demonstrates a high sensitivity of 84,000 $\mu C\,Gy_{air}^{-1}\,cm^{-2}$ together with a low X-ray detection limit of 7.6 $nGy_{air}\,s^{-1}$ for 8 keV X-ray, [16] which already significantly outperforms the commercial α-Se-based ones [8, 16]. However, one major hurdle that prevents the practical application of OIHP-based X-ray detectors is their ion migration issue, which is especially severe in iodine-based OIHPs like $CH_3NH_3PbI_3$ ($MAPbI_3$) due to the weaker chemical bond strength of Pb-I compared to Pb-Br and Pb-Cl [17–19]. The ion migration not only causes the dark current drift which increases the difficulty in signal reading and processing [20] but also leads to the formation of charge traps and even the decomposition of material [21, 22]. Although reducing the applied electric field can improve the bias stability of the device, it will sacrifice the collection efficiency of the charge carriers and hence the sensitivity of the device. Furthermore, the isotropic diffusion of the X-ray-generated carriers cannot be effectively inhibited with the small electric field, which eventually gives rise to the signal crosstalk between the adjacent pixels and hence impairs the X-ray imaging resolution. It is generally accepted that the major ion migration channel in OIHP SCs is through their surface, which contains a large amount of surface defects [17, 23]. Although the surface post treatment strategy has been widely used in perovskite solar cells to passivate the surface trap states, [24–28] it remains challenging to realize the complete suppression of ion migration in perovskite-based X-ray detectors. This is because in contrast to solar cells, the operation of X-ray detectors usually requires the application of large external bias in order to fully extract the X-ray-generated charge carriers from the thick active layer. In addition, the X-ray-generated carrier density in common X-ray detectors is usually several orders of magnitude lower than that in the solar cells under one sun illumination, which requires an ultralow surface trap density to avoid the photocurrent loss through surface recombination. Previously, the UV-ozone post treatment and the heteroepitaxial growth of BiOBr have been successfully used to passivate the defects in $MAPbBr_3$ SCs and $Cs_2AgBiBr_6$ wafers, respectively, to realize the high-performance X-ray detectors. [9, 29] However, it is still urgently desired to explore an effective surface passivation method that is applicable to $MAPbI_3$ SCs to suppress the ion migration under a large electric field.

Regarding the device structure, the present OIHP SC-based X-ray detectors mainly adopt the vertical sandwich-like structure [9, 11, 16, 30–33], while the devices with a coplanar-structure have seldom been reported. The major advantage of the coplanar-structure is that it differentiates the photosensitization length with the carrier transport distance. This is particularly advantageous for OIHP SC-based X-ray imaging sensors, which requires the preparation of large-area OIHP SC with preciously controlled thickness when adopting the vertical sandwich-like structure. In contrast, the charge collection efficiency of the coplanar-structure detector is insensitive to the active layer thickness (as long as it is larger than the attenuation length of the X-ray), which will greatly lower the requirement on the thickness uniformity of the perovskite SC and hence simplify the device fabrication procedure.

In this article, we show that the metallic lead defects on $MAPbI_3$ SCs can be effectively eliminated with atomistic surface passivation by a controllable surface self-assemble process of methylammonium iodide (MAI) on the SC surface without excess MAI layer formation, which dramatically increases the bias stability of a coplanar-structure X-ray detector due to the suppressed ion migration. The detectors with atomistic surface passivation exhibit a record-large sensitivity above 700,000 $\mu C\,Gy_{air}^{-1}\,cm^{-2}$ under a large electric field up to 100 $V\,mm^{-1}$ and are thus able to detect an ultralow X-ray dose rate down to 1.5 $nGy_{air}\,s^{-1}$. The demonstrated devices, combining high sensitivity, low detection limit, and the superior robustness under large external electric field, show huge potential to high-resolution and low-dose X-ray medical imaging in the future.

2. Results and Discussion

2.1. Atomistic Surface Passivation in $CH_3NH_3PbI_3$ SC X-Ray Detectors. The coplanar-structure $CH_3NH_3PbI_3$ SC X-ray detector was fabricated with a metal-semiconductor-metal architecture as shown in Figures 1(a)–1(c). The width of each finger of electrodes is approximately 50 μm, and the spacing between the anode and cathode is approximately 50 μm in interdigital electrodes, which was prepared simply by direct metal deposition through shadow masks on the SC surface, and does not require an expensive and complicated photolithography process. The device operation mechanism is schematically shown in Figure 1(b). The incident X-ray excites electrons and holes in the SC, which are separated by the applied external electric field and collected by the anode and cathode, respectively. Therefore, the charge collection efficiency is largely determined by the applied electric field. However, for regular OIHP-based detectors, usually, a small electric field is applied across the perovskite layer to avoid the ion migration effect for better operational stability. Although the use of SCs can eliminate the fast ion migration pathways caused by grain boundaries, the surface of the SC with a high density of defects can still behave as an ion migration channel, especially for the coplanar-structure device in which the electric field is located close to the crystal surface (Figure 1(d)). In our previous work, a significant passivation effect on the OIHP SC surface was proved by MAI treatment, which effectively recovered the surface damage of SCs with significantly suppressed surface trap density and longer carrier recombination lifetime and eventually led to efficient solar cell devices. [34] However, an excess of MAI, as shown in Figure 1(e), may introduce extra mobile ions on the SC surface, which is unfavorable in X-ray detectors which generally work under a much higher electric field than that of solar cells.

Here, the atomistic surface passivation, or an accurately controlled passivation of the SC surface without excess MAI layer formation (Figure 1(f)), was realized by a surface self-assemble process, in order to achieve surface passivation

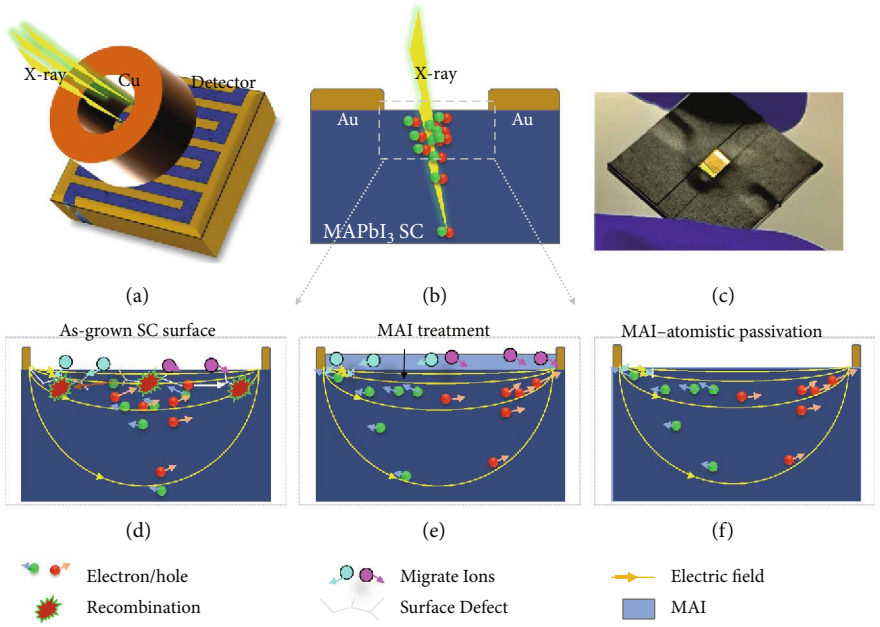

FIGURE 1: Schematic diagram of the device structure and working principle. (a, b) Top-view (a) and cross-sectional (b) schematic diagram of the coplanar-structure X-ray detector. (c) The photograph of a $MAPbI_3$ single crystal coplanar-structure X-ray detector. (d–f) Schematic diagram of the working principle of the X-ray detector with different surface treatments: (d) untreated, (e) MAI treatment, and (f) MAI-atomistic passivation.

and suppress ion migration simultaneously. The atomistic passivation was realized simply by using a diluted MAI solution to cover the surface of the as-grown crystals followed by selective dissolving of the unbonded dissociative MAI with an isopropanol washing process, which was an excellent solvent to MAI but harmless to perovskites. Based on the atomic force microscope (AFM) images shown in Figure S1, the root mean square (RMS) roughness values of the untreated, MAI-treated, and atomistic passivated SCs were 2.14 nm, 1.46 nm, and 1.42 nm, respectively, which indicated that different processing conditions on the SC surface did not affect their surface roughness obviously.

The atomistic surface passivation has proved to effectively passivate the surface defects and eliminate the excess MAI-rich layer based on the XPS measurement, which is sensitive to the surface properties of the specimen. As shown in Figures 2(a) and 2(b), there was plenty of metallic lead observed at the surface of as-grown $MAPbI_3$ SCs, which can be passivated by MAI treatment that was consistent with our previous results. [34]. However, after regular MAI treatment, the peak related to metallic lead was suppressed, while the peak related to MAI emerged in the C1s spectrum, which indicated that an excess MAI layer was formed [35]. In contrast, by using the atomistic passivation instead of regular MAI treatment, both the peaks related to MAI and metallic lead were effectively suppressed. This was because MAI can interact with unbonded metallic lead during self-assemble treatment, and the subsequent isopropanol washing procedure can take away the excess unbonded MAI without destroying the bonded MAI.

The atomistic surface passivation effect was further evidenced by the significantly reduced surface trap density of SCs with passivation treatment based on the space-charge-limited current (SCLC) measurement as shown in Figure 2(c). The electron-only devices with the symmetric lateral structure of Cu/BCP/C60/$MAPbI_3$ SC/C60/BCP/Cu were used for the SCLC measurement with the channel width of 50 μm. From the $I-V$ curve, we can obtain the trap filling threshold voltage for a gap-type structure by Geurst's SCLC model [36]:

$$V_T = \frac{\pi n_t L}{4\varepsilon_0 \varepsilon_r}, \tag{1}$$

where n_t is the surface trap density per unit area, ε_0 is the vacuum permittivity, ε_r is the relative dielectric constant of $MAPbI_3$ which equals to 32, [12] and L is the gap width. The surface trap density of SC with MAI treatment was suppressed from 1.63×10^{10} cm^{-2} to 5.68×10^{9} cm^{-2} and was further reduced to 1.8×10^{9} cm^{-2} after isopropanol washing.

The passivation effect can also be observed from the photoluminescence (PL) spectrum and time-resolved photoluminescence (TRPL) measurements as shown in Figures 2(d) and 2(e), respectively. The PL peak located at 774 nm for untreated SCs, and there was a 3 nm blueshift of the PL peak for SCs with MAI treatment ,which was ascribed to the reduction of the band tail states of the SC surface. When the excess MAI was washed away, the PL peak blueshifts by 5 nm compared to the untreated ones due to the further trap states suppression. [26, 37] In accordance with the PL peak shift, the full width at half maxima (FWHM) of PL spectrum of SCs with atomistic passivation was reduced to 39.5 nm in comparison to that of 43.3 nm and 44 nm of the untreated and MAI-treated ones, respectively. In addition,

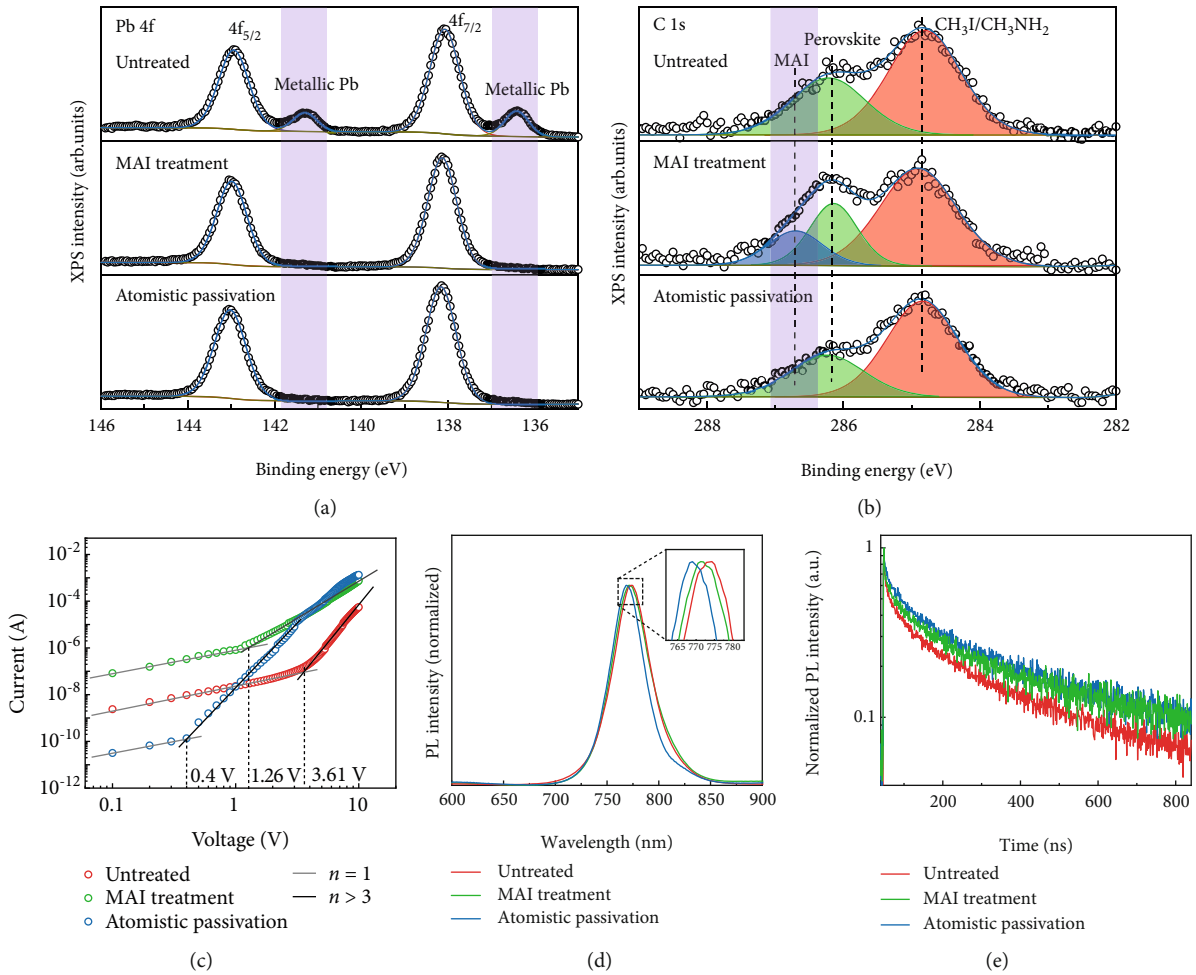

FIGURE 2: Atomistic surface passivation in $MAPbI_3$ SCs. (a, b) XPS spectra corresponding to (a) Pb-4f and (b) C-1s core levels of the $MAPbI_3$ SC surface with deferent treatments. (c) The SCLC measurement of the electron-only devices with different treatments. (d, e) The PL (d) and TRPL (e) spectra of the $MAPbI_3$ SC surface with different treatments.

from the single-log plots of the PL spectra (Figure S2), it was shown that the atomistic passivated SCs exhibited weaker band tail emission compared to the untreated and MAI-treated ones, indicating the significantly suppressed band tail states in the atomistic passivated SCs. The SCs with atomistic passivation also showed longer charge recombination lifetime (672.8 ns) than that of the untreated SCs (595.2 ns) and MAI-treated ones (655.2 ns), further confirming the trap passivation effect of the atomistic MAI treatment.

The effective passivation without introducing excess MAI significantly reduces the ion migration effect on the surface of SCs, which is directly evidenced by measuring the variation of activation energy (E_a) for the ion migration in $MAPbI_3$ SCs with different treatments. The ion migration activation energy is obtained from the conductivity change with temperature of the SCs, which is a well-established method to evaluate the ion migration behavior in halide perovskites. [38–40] In the lower temperature range, the ionization energy is ascribed to the free charges, because most ions are frozen to move at a low temperature. While the activation energy derived at the higher temperature range is mainly contributed by the activation of ion migration. E_a is determined by measuring the σ as a function of temperature under a 0.4 V μm^{-1} electrical field (Figure 3(a)). The activation energy can be extracted from the Nernst-Einstein relation [38]:

$$\sigma(T) = \left(\frac{\sigma_0}{T}\right) \exp\left(-\frac{E_a}{k_B T}\right), \tag{2}$$

where k_B is the Boltzmann constant, σ_0 is a constant, and T is temperature. For the SCs without surface treatment, the ion conductivity began to dominate the total conductivity above 285 K in the dark, with an E_a of 0.984 eV. In comparison, the conductivity of SCs with MAI treatment showed the transition point at 274 K with an E_a of 0.814 eV. When the excessive MAI was washed away, the transition temperature was significantly increased to 295 K with a much higher E_a of 1.784 eV, which means an effectively suppressed ion migration at the surface of SCs by atomistic surface passivation.

The suppressed ion migration in atomistic surface passivated SCs was further supported by observing the morphology

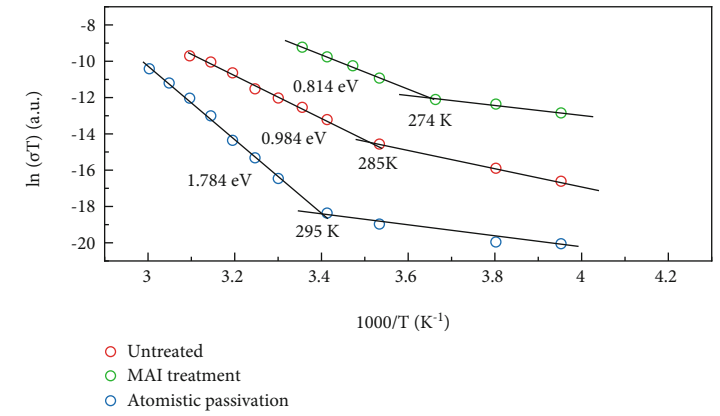

(a)

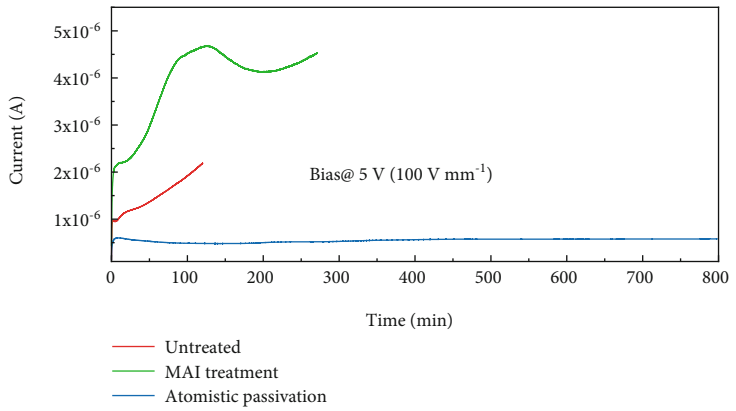

(b)

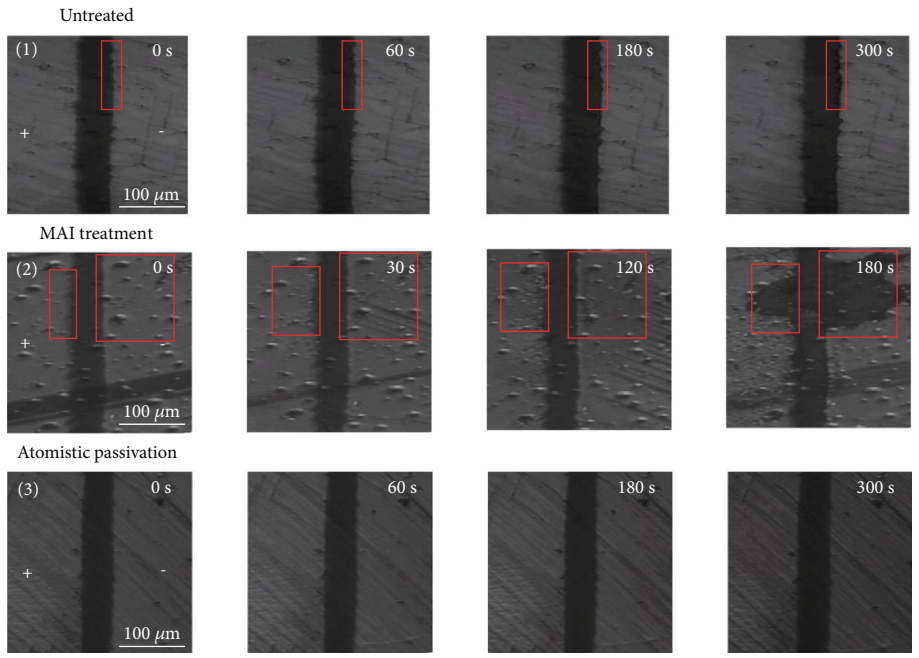

(c)

FIGURE 3: The characterization of the ion migration effect in $MAPbI_3$ SCs. (a) Temperature-dependent conductivity of the $MAPbI_3$ SC coplanar-structure devices in the dark. (b) The dark current as a function of time of the $MAPbI_3$ SC coplanar-structure devices with different treatments at a constant bias of 5 V. (c) Microscope images of $MAPbI_3$ single crystals with three treatment conditions under constantly applied bias (2 V μm^{-1}) at 25 mW cm^{-2}.

change of the crystal surface under a large electric field of $2\,V\,\mu m^{-1}$ with white light illumination of $25\,mW\,cm^{-2}$, since the severe ion migration will cause the surface damage of perovskites [41, 42]. It was shown in Figure 3(c) that there was weak damage near the electrode for the untreated one, while the surface damage was much severe when there was excess MAI on the SC surface. As a strong contrast, no observable damage can be found on the atomistic surface passivated SCs under the same biasing condition, indicating the remarkably suppressed ion migration which was in accordance with the above E_a measurement results.

To evaluate the bias stability of SCs with atomistic passivation, the dark current of the devices was tracked at 5 V bias ($100\,V\,mm^{-1}$) with different surface treatment conditions (Figure 3(b)). Also, the excess MAI induced a significantly increased ionic current, which increased quickly and then decreased, indicating the accelerated ion migration effect compared to the untreated SCs. In contrast, the dark current of the devices was significantly reduced after the atomistic passivation due to the elimination of the extra MAI. Moreover, the SC devices with atomistic surface passivation showed dramatically enhanced dark current stability, which displayed no degradation even after 800 minutes under continuous biasing.

2.2. X-Ray Detector Characterization. In view of the successful suppression of ion migration in $MAPbI_3$ SC-based coplanar-structure devices with atomistic surface passivation, and the large attenuation coefficient of the high-energy X-ray in $MAPbI_3$ SC (Figure S3), we exposed it to an X-ray source with an energy up to 50 keV and peak intensity at 22 keV to test its X-ray detection performance, which was collimated by a brass cylinder with a 2 mm diameter central hole in it. As shown in Figure 4(a), thanks to the excellent bias stability of the devices, a record-large sensitivity about $8 \times 10^5\,\mu C\,Gy_{air}^{-1}\,cm^{-2}$ was achieved with a bias of 5 V applied across the 50 μm wide channel under the X-ray dose rate of $20.3\,\mu Gy_{air}\,s^{-1}$. Since the device measurements were carried out in the air, it is crucial to evaluate the contribution from air ionization to the photocurrent of the devices. Therefore, we deposited the interdigitated Au electrodes with the same geometry on insulating glass substrates and measured the current response with successively tuning on and off the X-ray source. It was discovered that the photocurrent induced by air ionization was more than 4 orders of magnitudes smaller than that from the SC-based device (Figure S4), verifying the fidelity of the sensitivity of the device.

For X-ray detection application, noise is a very important figure of merit in addition to sensitivity, which was evaluated with a fast Fourier transform spectrum analyzer. We compared the noise spectra of the devices without and with atomistic MAI treatment and discovered that the MAI-atomistic-treated sample exhibited a decreased noise current of around $10^{-10}\,A\,Hz^{-1/2}$ which was is dominated by the $1/f$ noise in the low-frequency region (inset of Figure 4(a)). Since the $1/f$ noise is generally believed to originate from the charge trapping and detrapping processes in the conduction channel, the suppressed $1/f$ noise in the devices further confirms the remarkable surface passivation effect of MAI-atomistic surface treatment. [43–45]

The lowest detectable X-ray dose rate of the detectors is also an essential metric to evaluate the detection performance of the devices, especially for medical imaging application. To evaluate this, the X-ray dose rate was changed by adjusting the current of the X-ray tube or by adding Al foils as a filter. The photocurrent at different X-ray dose rates of the device at 5 V bias was shown in Figure 4(b). The average sensitivity of the device can be derived from the slope of the photocurrent density versus the X-ray dose rate, which was about $7.1 \times 10^5\,\mu C\,Gy_{air}^{-1}\,cm^{-2}$. Notably, the current signal generated under the X-ray dose rate down to $1.5\,nGy_{air}\,s^{-1}$ can be clearly differentiated from the noise current with the signal-to-noise ratio larger than 3, indicating its superior weak X-ray detection capability.

Figure 4(c) summarizes the sensitivity and the detection limit of various kinds of semiconductor-type X-ray detectors based on OIHPs and other materials. [7, 8, 15, 16, 29–31, 46–48] It is noted that the sensitivity of our devices is nearly 10 times larger than that of the best OIHP SC -X-ray detectors reported previously [16] and is also more than 35000-fold larger than that of the commercial α-Se X-ray detectors [8]. As a result of the significantly improved sensitivity, the detection limit of our devices is more than 5 times and 3600 times better than that of the OIHP SC and α-Se-based X-ray detectors, respectively [5, 8, 16], which displays great potential in ultralow-dose X-ray imaging application. The devices also exhibit good shelf stability with the sensitivity maintaining almost the same after storage in N_2-filled glovebox for over 650 h (Figure 4(d)), indicating that the long-term stability of the device could be guaranteed with sophisticated encapsulation.

The superior X-ray detection performance largely originates from the suppressed surface ion migration effect of the MAI atomistic passivated $MAPbI_3$ SCs, which enables us to apply a large electric field up to $100\,V\,mm^{-1}$ on the device for charge extraction that is more than 20- to 50-fold stronger than that of the previously reported OIHP SC-based devices [9, 31, 49]. This is particularly important for $MAPbI_3$ since it shows a much severer ion migration effect compared to $MAPbBr_3$ and $MAPbCl_3$. In addition, the electron-hole pair creation energy W of $MAPbI_3$, which can be calculated according to the empirical model $W = 1.43 + 2E_g$ (where E_g is the bandgap of the material) [50], is 77% of that of $MAPbBr_3$. Thus, the photogenerated carrier density can be increased by 30% in $MAPbI_3$ compared to $MAPbBr_3$ under the same X-ray irradiation condition. Furthermore, the passivation of surface traps on $MAPbI_3$SCs by atomistic passivation can elevate the charge extraction capacity under low-dose irradiation, which may otherwise be swallowed by the surface traps and thus deteriorate the detection limit of the device. Finally, the coplanar-structure device, which is firstly adopted in OIHP SC-based X-ray detectors, possesses the merit of differentiating the material thickness with the charge transport distance. This will facilitate the imaging array fabrication on the large-area $MAPbI_3$ SCs irrespective of their thickness uniformity. Also, the carrier confinement

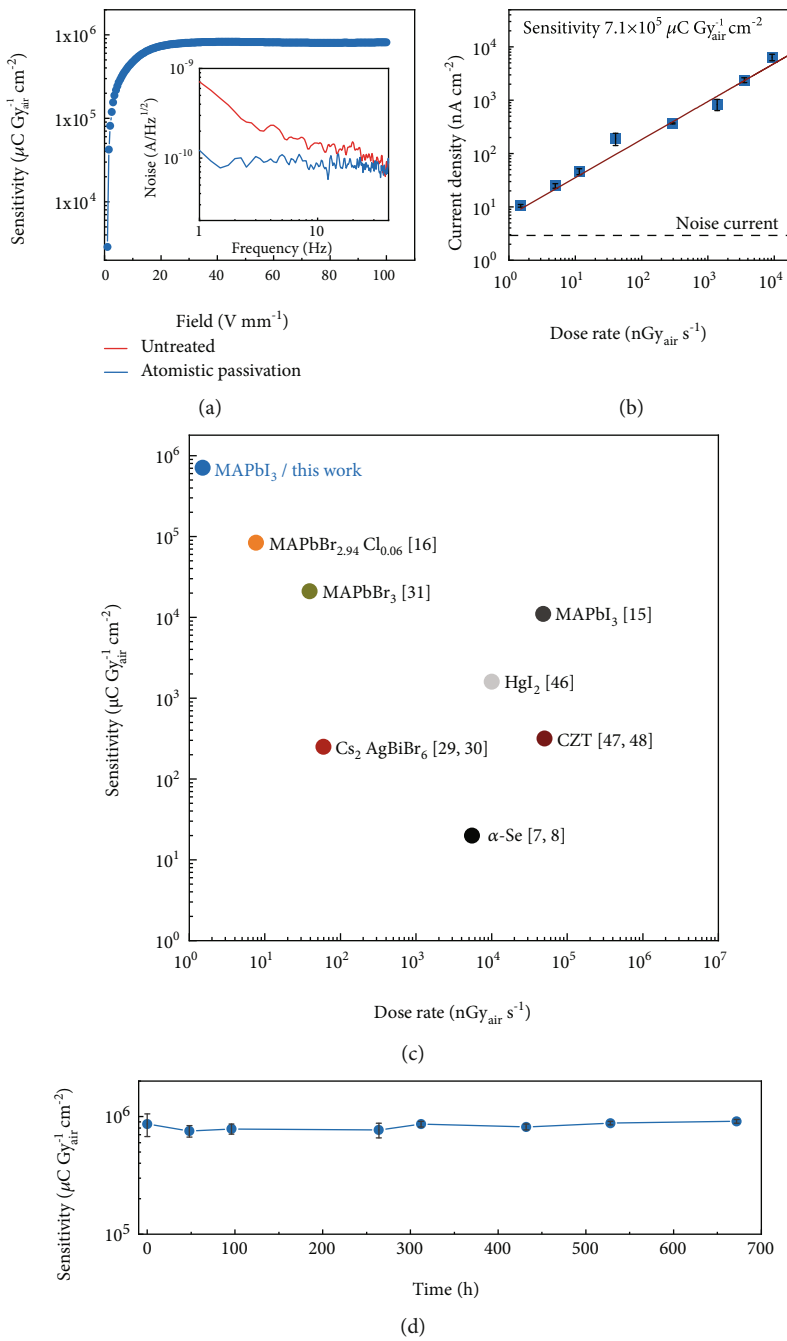

FIGURE 4: X-ray detection performance of the $MAPbI_3$ SC devices with atomistic surface passivation. (a) Sensitivity versus electric field of the devices. Inset: the noise spectra of the devices without and the atomistic surface treatment. (b) The current density as a function of incident dose rate of the devices. The dashed line is noise current of the devices. (c) Summary of the sensitivity and detection limit of various kinds of X-ray detectors with different active materials. [7, 8, 15, 16, 29–31, 46–48] (d) The sensitivity changes of the devices with the storage time.

capability of the coplanar-structure within the conductive channel can significantly inhibit the carrier diffusion and hence improve the X-ray imaging resolution in the future.

3. Conclusion

In summary, we have demonstrated a simple method to effectively passivate the metallic lead defects on the surface of $MAPbI_3$ SCs, which is achieved by coating a thin atomic layer of MAI on the SC surface. The passivation of the crystal not only suppresses the surface charge recombination but also significantly increases the ion migration activation energy, which allows a large electric field of 100 V mm^{-1} to be applied on the coplanar-structure device with improved dark current stability. As a result, the optimized coplanar-structure X-ray detectors possess both a high sensitivity above 700,000 $\mu C\,Gy_{air}^{-1}\,cm^{-2}$ and an ultralow X-ray detection limit down to 1.5 $nGy_{air}\,s^{-1}$, which remarkably outperform

those of the previously reported perovskite as well as commercial α-Se-based X-ray detectors. The superior device performance makes it promising for the ultralow-dose X-ray medical diagnostic applications in the future. In addition, the results presented here provide an encouraging strategy to improve the bias stability of the perovskite SCs, which could also be applied in other perovskite-based optoelectronic devices like solar cells and light emitting diodes.

4. Materials and Methods

4.1. Materials. The materials used are as follows: lead iodide (PbI_2) (99%, Born), methylammonium iodide (MAI) (99%, Born), gamma-butyrolactone (GBL) (99%, Aladdin), Fullerene-C60 (C60) (Xi'an Polymer Light), 2,9-dimethyl-4,7-diphenyl-1,10-phenanthroline (BCP) (Xi'an Polymer Light), and isopropanol (IPA) (≥99.5%, Sigma-Aldrich).

4.2. Growth of $MAPbI_3$ Single Crystal. The $MAPbI_3$ thin single crystals were grown by using the inverse temperature space-confined method in the hydrophobic substrates which were obtained by applying a hydrophobic reagent to the glass surface. Equal molars of PbI_2 and MAI are dissolved in GBL and prepared as a 1.5 M $MAPbI_3$ precursor solution and stirred for 2 hours at 70°C. The precursor solution was injected between the two hydrophobic substrates on the hot stage at 75°C, and then, the temperature was increased by 5°C every hour up to 120°C. The crystals were removed from the hot stage after growing to the suitable size.

4.3. Device Fabrication. To fabricate devices for SCLC measurement, 20 nm C60, 7.5 nm BCP, and 50 nm Cu were deposited sequentially on the surface of the SCs through a shadow mask with a 50 μm channel width. To prepare devices for E_a measurement, 50 nm thick Au electrodes with a 50 μm channel width were deposited on the surface of the SCs through a shadow mask. To fabricate X-ray detectors, 50 nm interdigital Au electrodes were deposited on the surface of the SCs through a shadow mask. For the MAI treatment, 1 mg mL^{-1} MAI solution in IPA was deposited on the SC surface by spin coating at 3000 r.p.m and then annealed at 50°C for 10 min on a hot plate. For the MAI-atomistic passivation, the excess MAI on the SC surface was washed away by spin coating IPA.

4.4. Material and Device Characterization. For the E_a, SCLC, and $I-t$ measurements of the SC devices, they were measured by a Keithley 2400 source meter in the N_2-filled glove box. The XPS measurement were conducted with ESCALAB 250Xi X-ray photoelectron spectrometer. The PL spectra were measured by an optical fiber spectrometer QE65 Pro (Ocean Optics, U.S.A.) with 365 nm LED as the excitation source. The TRPL spectra were obtained by a HORIBA Scientific Fluoromax-4P instrument with a 370 nm pulse laser as the excitation source. The AFM measurement was carried out by a Bruker FastScan AFM system.

The X-ray detectors were measured in the open air. An Amptek Mini-X2 tube was used as the X-ray source. The X-ray source was collimated by a brass cylinder with a 2 mm diameter central hole in it, and the X-ray detector was placed very close to the outlet of the X-ray source. The dose rate of the X-ray source was tuned by changing the tube current, as well as by adding aluminum foils with various thicknesses as the filters. The actual X-ray dose rate on the device was carefully calibrated with a Radcal Accu-Gold+ 10X6-180 ion chamber dosimeter, by placing the dosimeter at the same position as that of the device to be measured. The photocurrent and dark current of the devices were recorded with a Keithley 2400 source meter. Based on the measured photocurrent I, the X-ray dose rate D, and the X-ray spot area A, the sensitivity S can be calculated based on the equation: $S = I/AD$. The noise of the devices was measured with an Agilent 35670A dynamic signal analyzer and a SRS 570 current preamplifier.

Conflicts of Interest

The authors declare no competing financial interests.

Authors' Contributions

Y.L. Song and L.Q. Li contributed equally to this work. Q.F. Dong and Y.J. Fang supervised the project. Q.F. Dong conceived the idea and conducted the initial experiment. Y.L. Song contributed to the crystal preparation and device fabrication. Y.J. Fang and L.Q. Li carried out the characterization of X-ray detectors. L.Q. Li, Y.L. Song, W.H. Bi, M.W. Hao, Y.F. Kang, Z.S. Wang, A.R. Wang, H.M. Li, and X.H. Li contributed to the characterization of single crystals and devices. Q.F. Dong, Y.J. Fang, D.R. Yang, Y.L. Song, and L.Q. Li wrote the paper.

Acknowledgments

The authors acknowledge funding support from the National Natural Science Foundation of China (No. 21875089), the National Key Research and Development Program of China (No. 2018YFB2200105), the Science Fund for Creative Research Groups of the National Natural Science Foundation of China (No. 61721005), and the Fundamental Research Funds for the Central Universities of China (No. 2019QNA4009).

Supplementary Materials

Figure S1: AFM characterization of $MAPbI_3$ single crystal surface. The RMS values of the roughness of (a) untreated, (b) MAI treatment, and (c) atomistic passivation are 2.14 nm, 1.46 nm, and 1.42 nm, respectively. Figure S2: the single-log plots of the PL spectra. Figure S3: the attenuation coefficient of $MAPbI_3$ as a function of incident photon energy. Figure S4: the X-ray response of the device on insulating glass substrates measured by successively turning on and off the X-ray source with the dose rate of 20.3 $\mu Gy_{air}\, s^{-1}$, which corresponds to a sensitivity of about 16 $\mu C\, Gy_{air}^{-1}\, cm^{-2}$ that comes from the contribution of the air ionization. *(Supplementary Materials)*

References

[1] P. Büchele, M. Richter, S. F. Tedde et al., "X-ray imaging with scintillator-sensitized hybrid organic photodetectors," *Nature Photonics*, vol. 9, no. 12, pp. 843–848, 2015.

[2] A. Sakdinawat and D. Attwood, "Nanoscale X-ray imaging," *Nature Photonics*, vol. 4, no. 12, pp. 840–848, 2010.

[3] S. Kasap, J. B. Frey, G. Belev et al., "Amorphous and polycrystalline photoconductors for direct conversion flat panel x-ray image sensors," *Sensors*, vol. 11, no. 5, pp. 5112–5157, 2011.

[4] Y. Yamamoto and K. Shinohara, "Application of X-ray microscopy in analysis of living hydrated cells," *The Anatomical Record*, vol. 269, no. 5, pp. 217–223, 2002.

[5] D. J. Brenner, C. D. Elliston, E. J. Hall, and W. E. Berdon, "Estimated risks of radiation-induced fatal cancer from pediatric CT," *American Journal of Roentgenology*, vol. 176, no. 2, pp. 289–296, 2001.

[6] E. C. Lin, "Radiation risk from medical imaging," *Mayo Clinic Proceedings*, vol. 85, no. 12, pp. 1142–1146, 2010.

[7] H. Wei and J. Huang, "Halide lead perovskites for ionizing radiation detection," *Nature Communications*, vol. 10, no. 1, p. 1066, 2019.

[8] S. O. Kasap, "X-ray sensitivity of photoconductors: application to stabilized a-Se," *Journal of Physics D: Applied Physics*, vol. 33, no. 21, pp. 2853–2865, 2000.

[9] H. Wei, Y. Fang, P. Mulligan et al., "Sensitive X-ray detectors made of methylammonium lead tribromide perovskite single crystals," *Nature Photonics*, vol. 10, no. 5, pp. 333–339, 2016.

[10] S. Yakunin, D. N. Dirin, Y. Shynkarenko et al., "Detection of gamma photons using solution-grown single crystals of hybrid lead halide perovskites," *Nature Photonics*, vol. 10, no. 9, pp. 585–589, 2016.

[11] S. Yakunin, M. Sytnyk, D. Kriegner et al., "Detection of X-ray photons by solution-processed organic-inorganic perovskites," *Nature Photonics*, vol. 9, no. 7, pp. 444–449, 2015.

[12] Q. Dong, Y. Fang, Y. Shao et al., "Electron-hole diffusion lengths >175 μm in solution-grown CH3NH3PbI3single crystals," *Science*, vol. 347, no. 6225, pp. 967–970, 2015.

[13] J. Huang, Y. Shao, and Q. Dong, "Organometal trihalide perovskite single crystals: a next wave of materials for 25% efficiency photovoltaics and applications beyond?," *The Journal of Physical Chemistry Letters*, vol. 6, no. 16, pp. 3218–3227, 2015.

[14] Y. Liu, Z. Yang, D. Cui et al., "Two-inch-sized perovskite $CH_3NH_3PbX_3$ (X = Cl, Br, I) crystals: growth and characterization," *Advanced Materials*, vol. 27, no. 35, pp. 5176–5183, 2015.

[15] Y. C. Kim, K. H. Kim, D. Y. Son et al., "Printable organometallic perovskite enables large-area, low-dose X-ray imaging," *Nature*, vol. 550, no. 7674, pp. 87–91, 2017.

[16] H. Wei, D. DeSantis, W. Wei et al., "Dopant compensation in alloyed $CH_3NH_3PbBr_{3-x}Cl_x$ perovskite single crystals for gamma-ray spectroscopy," *Nature Materials*, vol. 16, no. 8, pp. 826–833, 2017.

[17] Y. Yuan and J. Huang, "Ion migration in organometal trihalide perovskite and its impact on photovoltaic efficiency and stability," *Accounts of Chemical Research*, vol. 49, no. 2, pp. 286–293, 2016.

[18] T. Zhang, C. Hu, and S. Yang, "Ion migration: a "double-edged sword" for halide-perovskite-based electronic devices," *Small Methods*, vol. 4, no. 5, article 1900552, 2020.

[19] R. Long and O. V. Prezhdo, "Dopants control electron-hole recombination at perovskite–TiO2 interfaces: Ab initio time-domain study," *ACS Nano*, vol. 9, no. 11, pp. 11143–11155, 2015.

[20] Y. C. Zhao, W. K. Zhou, X. Zhou, K. H. Liu, D. P. Yu, and Q. Zhao, "Quantification of light-enhanced ionic transport in lead iodide perovskite thin films and its solar cell applications," *Light: Science & Applications*, vol. 6, no. 5, article e16243, 2017.

[21] Y. Yuan, Q. Wang, Y. Shao et al., "Electric-field-driven reversible conversion between methylammonium lead triiodide perovskites and lead iodide at elevated temperatures," *Advanced Energy Materials*, vol. 6, no. 2, article 1501803, 2016.

[22] T. Leijtens, E. T. Hoke, G. Grancini et al., "Mapping electric field-induced switchable poling and structural degradation in hybrid lead halide perovskite thin films," *Advanced Energy Materials*, vol. 5, no. 20, article 1500962, 2015.

[23] T. Wu, M. Ahmadi, and B. Hu, "Giant current amplification induced by ion migration in perovskite single crystal photodetectors," *Journal of Materials Chemistry C*, vol. 6, no. 30, pp. 8042–8050, 2018.

[24] D. Luo, W. Yang, Z. Wang et al., "Enhanced photovoltage for inverted planar heterojunction perovskite solar cells," *Science*, vol. 360, no. 6396, pp. 1442–1446, 2018.

[25] Q. Jiang, Y. Zhao, X. Zhang et al., "Surface passivation of perovskite film for efficient solar cells," *Nature Photonics*, vol. 13, no. 7, pp. 460–466, 2019.

[26] Y. Shao, Z. Xiao, C. Bi, Y. Yuan, and J. Huang, "Origin and elimination of photocurrent hysteresis by fullerene passivation in $CH_3NH_3PbI_3$ planar heterojunction solar cells," *Nature Communications*, vol. 5, no. 1, p. 5784, 2014.

[27] X. Xiao, C. Bao, Y. Fang et al., "Argon plasma treatment to tune perovskite surface composition for high efficiency solar cells and fast photodetectors," *Advanced Materials*, vol. 30, no. 9, article 1705176, 2018.

[28] W. Q. Wu, Z. Yang, P. N. Rudd et al., "Bilateral alkylamine for suppressing charge recombination and improving stability in blade-coated perovskite solar cells," *Science Advances*, vol. 5, no. 3, article eaav8925, 2019.

[29] B. Yang, W. Pan, H. Wu et al., "Heteroepitaxial passivation of $Cs_2AgBiBr_6$ wafers with suppressed ionic migration for X-ray imaging," *Nature Communications*, vol. 10, no. 1, article 1989, 2019.

[30] W. Pan, H. Wu, J. Luo et al., "$Cs_2AgBiBr_6$ single-crystal X-ray detectors with a low detection limit," *Nature Photonics*, vol. 11, no. 11, pp. 726–732, 2017.

[31] W. Wei, Y. Zhang, Q. Xu et al., "Monolithic integration of hybrid perovskite single crystals with heterogenous substrate for highly sensitive X-ray imaging," *Nature Photonics*, vol. 11, no. 5, pp. 315–321, 2017.

[32] S. Shrestha, R. Fischer, G. J. Matt et al., "High-performance direct conversion X-ray detectors based on sintered hybrid lead triiodide perovskite wafers," *Nature Photonics*, vol. 11, no. 7, pp. 436–440, 2017.

[33] F. Yao, J. Peng, R. Li et al., "Room-temperature liquid diffused separation induced crystallization for high-quality perovskite single crystals," *Nature Communications*, vol. 11, no. 1, p. 1194, 2020.

[34] Y. Song, W. Bi, A. Wang, X. Liu, Y. Kang, and Q. Dong, "Efficient lateral-structure perovskite single crystal solar cells with high operational stability," *Nature Communications*, vol. 11, no. 1, p. 274, 2020.

[35] Z. Hawash, S. R. Raga, D. Y. Son, L. K. Ono, N. G. Park, and Y. Qi, "Interfacial modification of perovskite solar cells using an ultrathin MAI layer leads to enhanced energy level alignment, efficiencies, and reproducibility," *The Journal of Physical Chemistry Letters*, vol. 8, no. 17, pp. 3947–3953, 2017.

[36] R. Zuleeg and P. Knoll, "Space-charge-limited currents in heteroepitaxial films of silicon grown on sapphire," *Applied Physics Letters*, vol. 11, no. 6, pp. 183–185, 1967.

[37] Y. Lin, L. Shen, J. Dai et al., "π-conjugated Lewis base: efficient trap-passivation and charge-extraction for hybrid perovskite solar cells," *Advanced Materials*, vol. 29, no. 7, article 1604545, 2017.

[38] S. Yang, S. Chen, E. Mosconi et al., "Stabilizing halide perovskite surfaces for solar cell operation with wide-bandgap lead oxysalts," *Science*, vol. 365, no. 6452, pp. 473–478, 2019.

[39] Y. Yuan, J. Chae, Y. Shao et al., "Photovoltaic switching mechanism in lateral structure hybrid perovskite solar cells," *Advanced Energy Materials*, vol. 5, no. 15, article 1500615, 2015.

[40] X. Xiao, J. Dai, Y. Fang et al., "Suppressed ion migration along the in-plane direction in layered perovskites," *ACS Energy Letters*, vol. 3, no. 3, pp. 684–688, 2018.

[41] Z. Xiao, Y. Yuan, Y. Shao et al., "Giant switchable photovoltaic effect in organometal trihalide perovskite devices," *Nature Materials*, vol. 14, no. 2, pp. 193–198, 2015.

[42] S. Bai, P. da, C. Li et al., "Planar perovskite solar cells with long-term stability using ionic liquid additives," *Nature*, vol. 571, no. 7764, pp. 245–250, 2019.

[43] Y. Fang and J. Huang, "Resolving weak light of sub-picowatt per square centimeter by hybrid perovskite photodetectors enabled by noise reduction," *Advanced Materials*, vol. 27, no. 17, pp. 2804–2810, 2015.

[44] L. Wan, X. Shao, Y. Ma et al., "Dark current and 1/f noise characteristics of $In_{0.74}Ga_{0.26}As$ photodiode passivated by SiN_x/Al_2O_3 bilayer," *Infrared Physics & Technology*, vol. 109, article 103389, 2020.

[45] H. Zmuda, R. A. Soref, P. Payson, S. Johns, and E. N. Toughlian, "Photonic beamformer for phased array antennas using a fiber grating prism," *IEEE Photonics Technology Letters*, vol. 9, no. 2, pp. 241–243, 1997.

[46] G. Zentai, L. D. Partain, R. Pavlyuchkova et al., "Mercuric iodide and lead iodide x-ray detectors for radiographic and fluoroscopic medical imaging," in *Medical Imaging 2003: Physics of Medical Imaging, Pts 1 And 2*, pp. 77–91, San Diego, California, United States, 2003.

[47] Y. M. Ivanov, V. M. Kanevsky, V. F. Dvoryankin et al., "The possibilities of using semi-insulating CdTe crystals as detecting material for X-ray imaging radiography," *Physica Status Solidi (C)*, no. 3, pp. 840–844, 2003.

[48] R. Bellazzini, G. Spandre, A. Brez, M. Minuti, M. Pinchera, and P. Mozzo, "Chromatic X-ray imaging with a fine pitch CdTe sensor coupled to a large area photon counting pixel ASIC," *Journal of Instrumentation*, vol. 8, no. 2, pp. C02028–C02028, 2013.

[49] R. Zhuang, X. Wang, W. Ma et al., "Highly sensitive X-ray detector made of layered perovskite-like $(NH_4)_3Bi_2I_9$ single crystal with anisotropic response," *Nature Photonics*, vol. 13, no. 9, pp. 602–608, 2019.

[50] R. Devanathan, L. R. Corrales, F. Gao, and W. J. Weber, "Signal variance in gamma-ray detectors—a review," *Nuclear Instruments and Methods in Physics Research A*, vol. 565, no. 2, pp. 637–649, 2006.